

Chapter 6

Tests of QED

In the previous chapter elements of the quantum electrodynamics theory are discussed. We now turn to precision tests of the theory which usually consist in the measurement of the electromagnetic fine structure constant α in different systems. Experimental results are compared with theoretical predictions. The validation process requires very high precision in both measurements and theoretical calculations. QED is then confirmed to the extent that these measurements of α from different physical sources agree with each other. The most stringent test of QED is given by the measurement of the electron magnetic moment. However, several other experimental tests have been performed in different energy ranges and systems:

- Low energy range, accessible with small experiments;
- High energy range, accessible with particle colliders (e.g. e^+e^- colliders);
- Condensed matter systems (quantum Hall effect, Josephson effect).

As we will see, the achieved precision makes QED one of the most accurate physical theories constructed so far.

6.1 Measurement of the electron anomalous magnetic moment

6.1.1 Electron magnetic moment

A rotating electrically charged body creates a magnetic dipole. In classical analogy, this is also the case for the spinning electron. External magnetic fields exert a torque on the electron magnetic moment. Electrons have an *intrinsic magnetic moment* μ , related to

their spin s :

$$\mu = -g \frac{e}{2m} s = -\frac{g}{2} \frac{e}{2m} \quad (6.1)$$

where e is the unit charge and m the electron mass. In the case of electrons the magnetic moment is anti-parallel to the spin. The g -factor is equal to 2, as calculated from Dirac's equation:

$$a \equiv \frac{g - 2}{2} = 0.$$

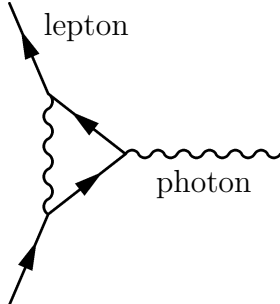
Corrections to the g -factor are given by higher order QED contributions as well as hadronic and weak interactions. There could be additional contributions from physics beyond the Standard Model (SM):

$$\frac{g}{2} = 1 + a_{\text{QED}}(\alpha) + a_{\text{hadronic}} + a_{\text{weak}} + a_{\text{new}}.$$

When adding the corrections we usually talk of the *anomalous magnetic moment* of the electron.

6.1.2 QED: higher order corrections

The one-loop corrections to the magnetic moment are due to vacuum fluctuation and polarization effects. A corresponding diagram is for example



The textbook calculation of the one-loop corrections gives corrections $\sim 10^{-3}$ (see [14, pp. 189]):

$$a = \frac{\alpha}{2\pi} \approx 0.0011614.$$

Hadronic and weak interactions are calculated (within the SM) to be very small and negligible, respectively.

As we will see, the precision achieved by experimental results needs QED predictions with α^4 precision.

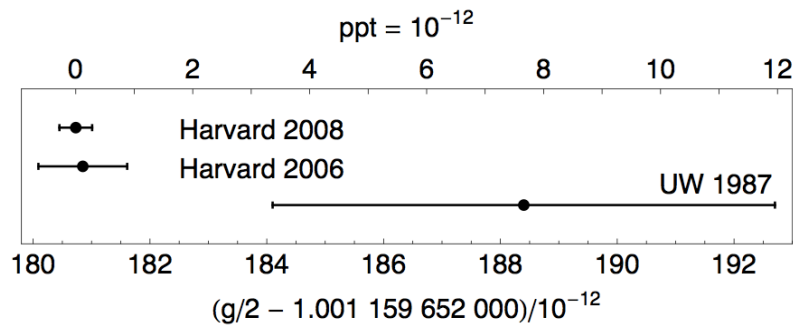


Figure 6.1: *Most accurate measurements of the electron $g/2$.* Source: [16, p. 177].

6.1.3 $g/2$ measurements

Nowadays the precision of the $g/2$ measurements is below 10^{-12} as is shown in Fig. 6.1. The latest measurements are 15 times more precise than the previous result which stood for about 20 years. As one can see in Fig. 6.1, the latest value is shifted by 1.7 standard deviations with respect to the previous result from 1987.

So, how did we get to this astonishing precision?

6.1.3.1 Experiment

The main ingredients of the experiment are:

- *Single-electron quantum cyclotron*
A Penning trap suspends and confines the electron in an atom-like state.
- *Fully resolved cyclotron and spin energy levels*
Accurate measurements of the resonant frequencies of driven transitions between the energy levels of this homemade atom—an electron bound to the trap—reveals the electron magnetic moment in units of Bohr magnetons, $g/2$.
- *Detection sensitivity sufficient to detect one quantum transitions*
Frequency detection sensitivity in the radio and microwave region.

The Penning trap confines electrons by using a strong vertical magnetic field B for radial confinement and a quadrupole electric field for axial confinement (see Fig. 6.2(a)). The magnetic field is produced by a solenoid while the electric field is produced by three electrodes: one ring and two endcaps. A sketch of the electron trajectory is shown in Fig. 6.2(b). The trajectory in the radial plane is characterized by two frequencies: The magneton frequency ω_- and the modified cyclotron frequency ω_+ . The cyclotron frequency is then $\omega = \omega_+ + \omega_-$. Since there is also a low-frequency oscillation in the z -direction, the overall trajectory has the shown form.

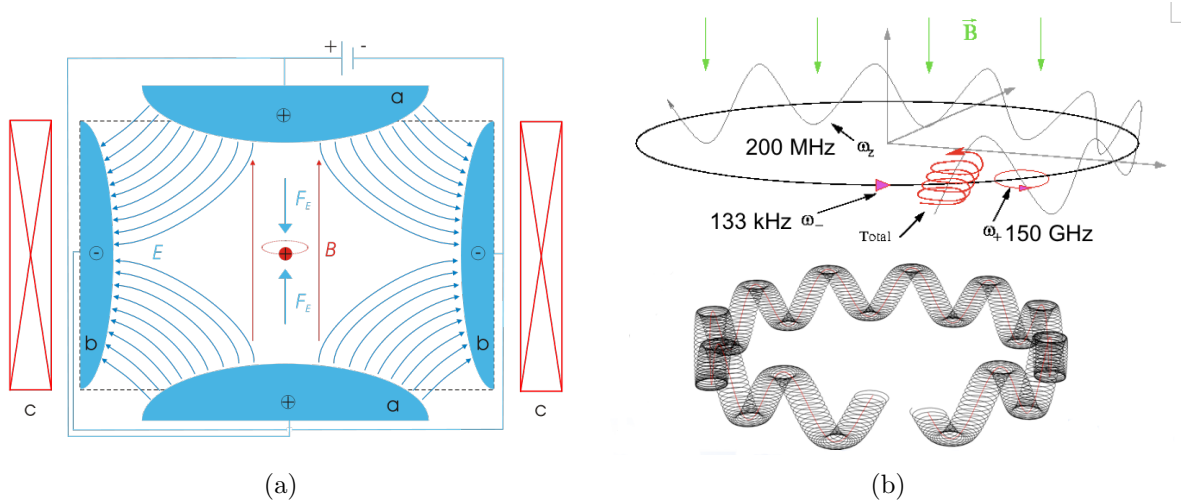


Figure 6.2: Sketch of the fields and the electron trajectory in a Penning trap. Confinement is achieved by a vertical magnetic field and a quadrupole electric field. Source: [17]. (a) The magneton frequency ω_- and the modified cyclotron frequency ω_+ contribute to the electron trajectory as well as a low-frequency oscillation in z -direction. (b)

A non-relativistic electron in a magnetic field has the following energy levels:¹

$$E(n, m_s) = \frac{g}{2} h\nu_c m_s + \left(n + \frac{1}{2} \right) h\nu_c \quad (6.2)$$

depending on the cyclotron frequency

$$\nu_c = \frac{eB}{2\pi m} \quad (6.3)$$

and on the spin frequency

$$\nu_s = \frac{g}{2} \nu_c = \frac{g}{2} \frac{eB}{2\pi m}. \quad (6.4)$$

Here n is the principal quantum number and m_s the spin quantum number. Eq. (6.4) yields

$$\frac{g}{2} = \frac{\nu_s}{\nu_c} = 1 + \frac{\nu_s - \nu_c}{\nu_c} \equiv 1 + \frac{\nu_a}{\nu_c}.$$

Since ν_s and ν_c differ only by one part per 10^3 , measuring ν_a and ν_c to a precision of one part per 10^{10} gives $g/2$ to one part per 10^{13} .

This technique of measuring $g/2$ has two main advantages:

¹See e. g. [18, § 112].

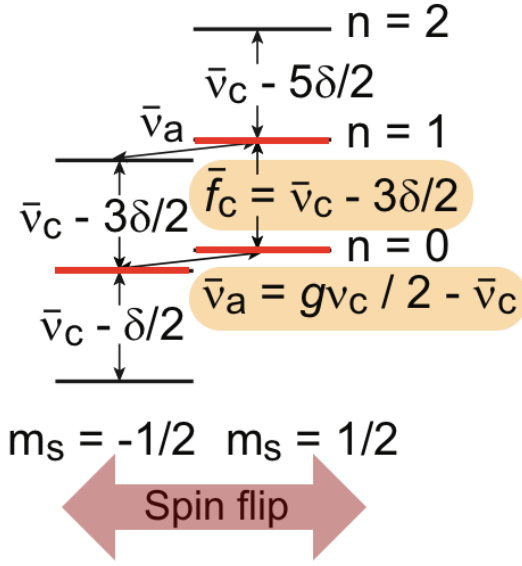


Figure 6.3: Lowest cyclotron and spin levels of an electron in a Penning trap. Source: [16, p. 180, modified].

1. One can measure the ratio of two frequencies to very high precision.
2. Since the B field appears in both numerator and denominator (see Eq. (6.4)), the dependence on the magnetic field cancels in the ratio.

Including the relativistic corrections, Eq. (6.2) is modified and the energy levels are given by:

$$E(n, m_s) = \frac{g}{2} h \nu_c m_s + \left(n + \frac{1}{2} \right) h \bar{\nu}_c - \underbrace{\frac{1}{2} h \delta \left(n + \frac{1}{2} + m_s \right)^2}_{\text{relativistic correction term}}$$

where $\bar{\nu}_c$ denotes the cyclotron frequency, shifted due to the Penning trap. Higher states are excited via microwave radiation. The experiment measures the following transition frequencies (see Fig. 6.3):

$$\begin{aligned} \bar{f}_c &\equiv \bar{\nu}_c - \frac{3}{2}\delta, \text{ corresponding to } (n, m_s) = (1, 1/2) \rightarrow (0, 1/2) \text{ and} \\ \bar{\nu}_a &\equiv \frac{g}{2} \nu_c - \bar{\nu}_c, \text{ corresponding to } (0, 1/2) \rightarrow (0, -1/2) \end{aligned}$$

with the cyclotron frequency $\nu_c \sim 150$ GHz.

A sketch of the experimental setup is shown in Fig. 6.4(a) and 6.4(b). A Penning trap is used to artificially bind the electron in an orbital state. For confinement, a high voltage

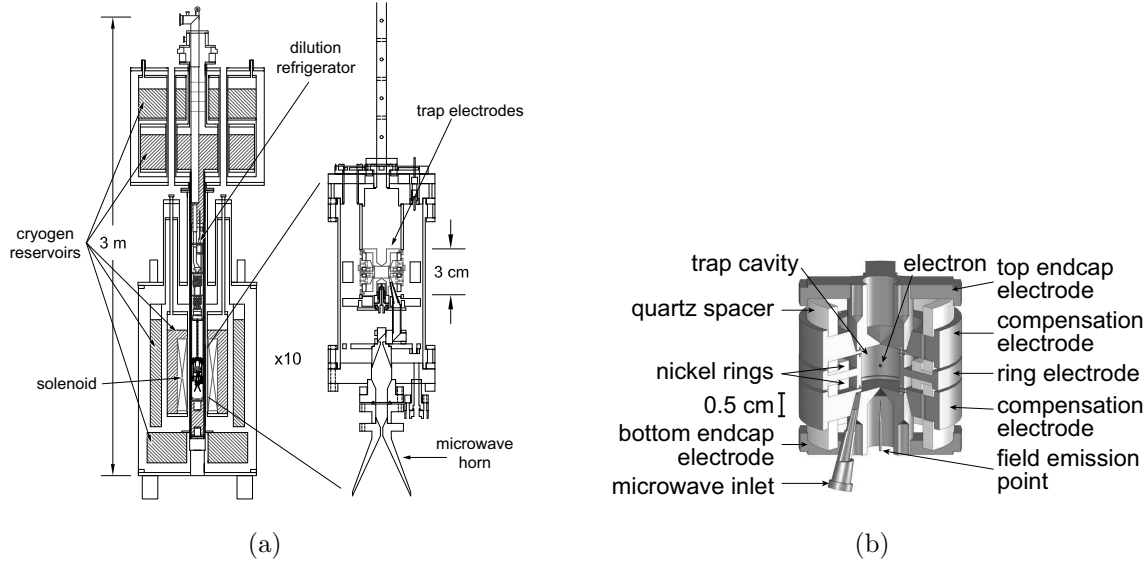


Figure 6.4: *Sketch of the experimental setup.* Overview of experimental apparatus. Source: [16, p. 185]. (a) The Penning trap cavity is used to confine a single electron and to inhibit spontaneous emission. Source: [16, p. 182]. (b)

(100 V) is applied between the cylindric and endcap contacts. Since $\nu_c \propto B$ (see Eq. (6.3)), a high magnetic field (5 T) is necessary to increase the spacing between the cyclotron energy levels. And finally, because the probability to occupy the orbital ground state is proportional to the Boltzmann factor,

$$\exp\left(-\frac{h\bar{\nu}_c}{k_B T}\right),$$

very low temperatures (100 mK) are needed.

In analyzing the results of Penning trap measurements, one has to correct for the frequency shifts due to the cavity. This can be done by measuring at various frequencies (see Fig. 6.5(a)). The result for $g/2$ given in [16] is

$$g/2 = 1.001\ 159\ 652\ 180\ 73\ (28) \quad [0.28 \text{ ppt}]. \quad (6.5)$$

6.1.3.2 Theoretical predictions

The QED calculations provide the prediction for $g/2$ up to the fifth power of α :

$$\frac{g}{2} = 1 + C_2 \left(\frac{\alpha}{\pi}\right) + C_4 \left(\frac{\alpha}{\pi}\right)^2 + C_6 \left(\frac{\alpha}{\pi}\right)^3 + C_8 \left(\frac{\alpha}{\pi}\right)^4 + C_{10} \left(\frac{\alpha}{\pi}\right)^5 + \dots + a_{\text{hadronic}} + a_{\text{weak}} \quad (6.6)$$

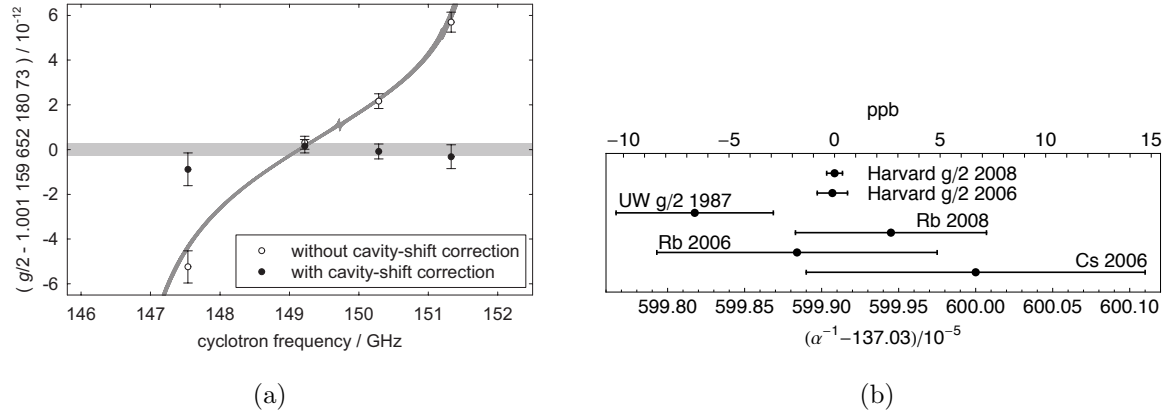


Figure 6.5: $g/2$ and fine structure constant. Four measurements of $g/2$ without (open) and with (filled) cavity-shift corrections. The light gray uncertainty band shows the average of the corrected data. The dark gray band indicates the expected location of the uncorrected data given the result in Eq. (6.5) and including only the cavity-shift uncertainty. Source: [16, p. 201]. (a) The most precise determinations of α . Source: [19, p. 264]. (b)

where

$$\begin{aligned} C_2 &= 0.500\,000\,000\,000\,00 \text{ (exact)} \\ C_4 &= -0.328\,478\,444\,002\,90 \text{ (60)} \\ C_6 &= 1.181\,234\,016\,827 \text{ (19)} \\ C_8 &= -1.914\,4 \text{ (35)} \\ C_{10} &= 0.0 \text{ (4.6)} \\ a_{\text{hadronic}} &= 1.682(20) \cdot 10^{-12}. \end{aligned}$$

From Eq. (6.6) and the theoretical predictions we can on the one hand measure the coupling constant α (see Fig. 6.5(b)):

$$\alpha^{-1} = 137.035\ 999\ 084\ (33)\ (39) \quad [0.24 \text{ ppb}][0.28 \text{ ppb}] \\ = 137.035\ 999\ 084\ (51) \quad [0.37 \text{ ppb}]$$

and on the other hand, we can compare the measured $g/2$ with the expectation using α from other measurements

$$g(\alpha)/2 = 1.001\ 159\ 652\ 177\ 60\ (520) \quad [5.2 \text{ ppt}] \text{ (predicted).}$$

6.2 High energy tests

6.2.1 e^+e^- colliders

In addition to the low-energy experiments, QED has been tested also in high energy e^+e^- collisions [20, 21, 22].

We discuss here the following reactions:

- Bhabha scattering : $e^+e^- \rightarrow e^+e^-$
- Lepton pair production : $e^+e^- \rightarrow \mu^+\mu^-, \tau^+\tau^-$
- Hadronic processes : $e^+e^- \rightarrow q\bar{q} \rightarrow \text{hadrons}$

The energy range $12 \text{ GeV} \leq \sqrt{s} \leq 47 \text{ GeV}$ was investigated with the PETRA accelerator at DESY (Hamburg). High energy ranges ($90 \text{ GeV} \leq \sqrt{s} \leq 200 \text{ GeV}$) were covered by the LEP collider at CERN (Geneva). However, electroweak contributions to the cross-sections, like the one shown in Fig. 6.6, become considerable at these energies. Intermediate energies were covered by TRISTAN and SLC. Table 6.1 gives an overview of the e^+e^- colliders.

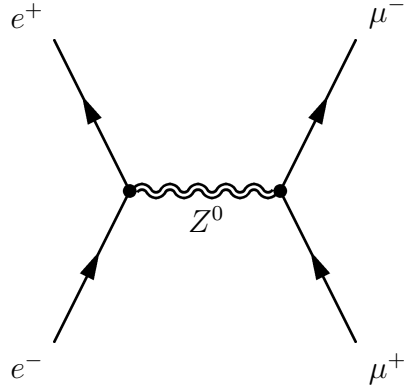


Figure 6.6: Electroweak contribution to $\mathcal{M}_{fi}(e^+e^- \rightarrow \mu^+\mu^-)$ at high energies.

The PETRA collider is shown in Fig. 6.7 as an example.

As an example for a typical detector we take a look at JADE (Figs. 6.8 and 6.9), using the same numbering as in the figure.

1. Beam pipes counters.
2. End plug lead glass counters.
3. Pressure tank.

Accelerator	Experiment(s)	\sqrt{s} [GeV]	\mathcal{L}_{int} [pb^{-1}]
SPEAR	SPEAR	2-8	-
PEP	ASP, DELCO, HRS, MARK II, MAC	0-29	300
PETRA	JADE, MARK J, PLUTO, TASSO, CELLO	12-47	20
TRISTAN	TRISTAN	50-60	20
SLC	MARK II, SLD	90	25
LEP	ALEPH, DELPHI, OPAL, L3	90-200	200 700

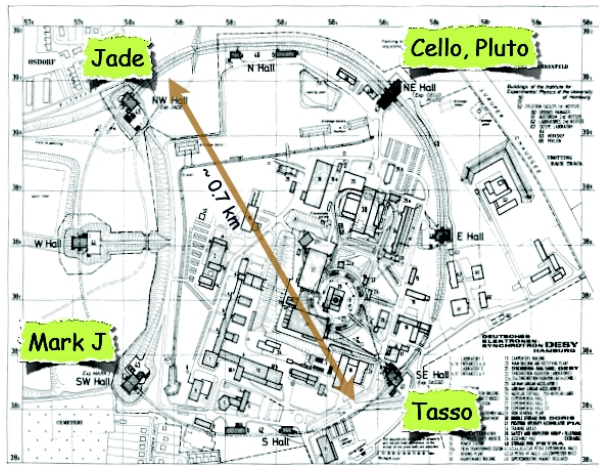
Table 6.1: Table of e^+e^- colliders

Figure 6.7: PETRA storage ring

4. *Muon chambers.* Detect muons.
5. *Jet chambers.* Records the trajectories of the produced particles.
6. *Time of flight counters.* Measure the time necessary for the particle to get from the collision center and thus its velocity.
7. *Coil.* Produces a magnetic field of 0.5 [T] parallel to the beam in the central region to measure the momentum of the particles by providing the curvature of their trajectories.
8. *Central lead glass counters.*
9. *Magnet yoke.*
10. *Muon filter.*
11. *Removable end plug.*

12. Beam pipe.
13. Tagging counter.
14. Mini beta quadrupole. Focus the beam to increase the luminosity of the beam in the experiment.
15. Moving devices.

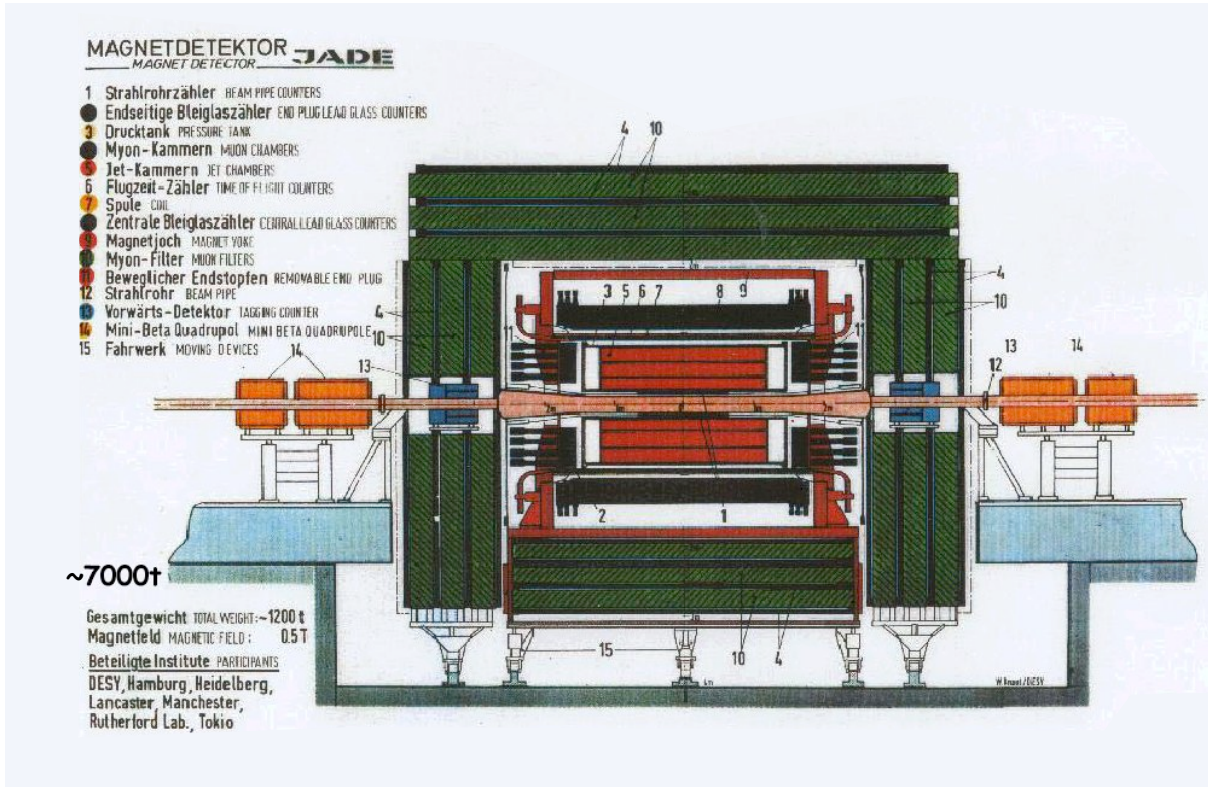


Figure 6.8: JADE detector : schematics

6.2.2 Detector elements

In order to help identify the particles produced in a collision (or their decay product) we can determine their charge and invariant mass using the methods presented in chapter 4. This measurement proceeds mostly in the inner part of the detector, see Fig. 4.15, by means of drift chambers or silicon trackers. If some of the produced particles are long living (i.e. are stable or decay weakly), this setup gives also the possibility to detect a decay vertex.

Further away from the beam axis are the **calorimeters**, whose function is to stop the particles and measure the energy they deposit. There are mostly two types of calorimeters:

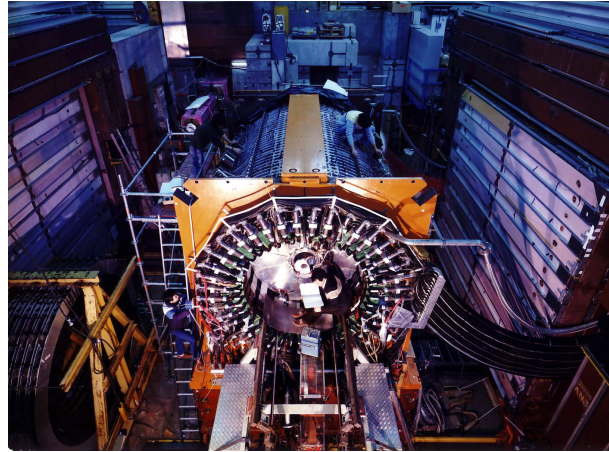


Figure 6.9: JADE detector

electromagnetic and hadronic. The angular resolution is limited by the size of each detector cell. Calorimeters are also able to measure neutral particles while the tracking devices described above can only detect charged particles.

Electromagnetic calorimeters stop and measure the energy of electrons, positrons and photons. All electromagnetically interacting particles leave at least a part of their energy in this detector part.

Hadronic calorimeters stop and measure the energy of hadrons, e.g. protons, neutrons and pions. Muons and antimuons are not stopped but leave some energy. Most modern experiments are also surrounded by **muon detectors** in order to distinguish the energy deposit of low energetic hadrons from the one of muons. Since it is practically impossible to stop muons, this last detector records the direction of passage of muons and, eventually, their momentum.

Fig. 6.10 shows the schematic view of the different signal hits for different types of particles. The energy deposit is usually depicted by a histogram.

- *Electron signature.* Electrons leave a curved trace in the inner tracking detector and deposit all their energy in the electromagnetic calorimeter, where they are completely stopped. There is hence no signal stemming from electrons in detectors further away from the collision point.
- *Hadron signature.* Charged hadrons leave a trace in the inner detector (curved by the magnetic field), – whereas uncharged hadrons do not –, deposit a part of their energy in the electromagnetic calorimeter and the rest of their energy in the hadronic calorimeter.

- *Muon signature.* Muons leave a curved trace in the inner detector and deposit some energy in the electromagnetic and hadronic calorimeters without being stopped, and then leave a signal in the muon detector.
- *Photon signature.* Photons do not leave a trace in the inner detector and are stopped in the electromagnetic calorimeter.

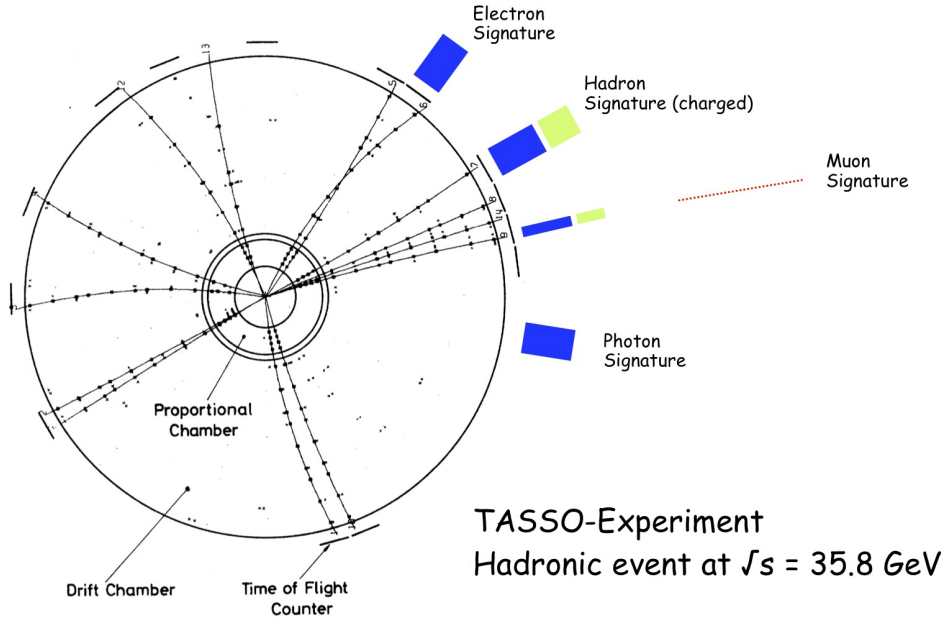


Figure 6.10: Event reconstruction principle

6.2.3 Cross section measurement

To measure a cross section we divide the measured number of events N by the integrated luminosity at that energy $\mathcal{L}(s)$,

$$\sigma(s) = \frac{N}{\mathcal{L}(s)}. \quad (6.7)$$

The last one is measured by counting the events occurring at small scattering angles and using the relation,

$$\sigma_{ee,\gamma\gamma}^{\text{theo}} = \frac{N(1 - b)}{(\varepsilon A) \cdot \mathcal{L}}, \quad (6.8)$$

where A and b depend on the detector geometry, while ε is the efficiency (the probability to measure a particle, if it hits the detector).

Fig. 6.11 shows a typical integrated luminosity spectrum over the energy range $0 - 47 \text{ GeV}$.

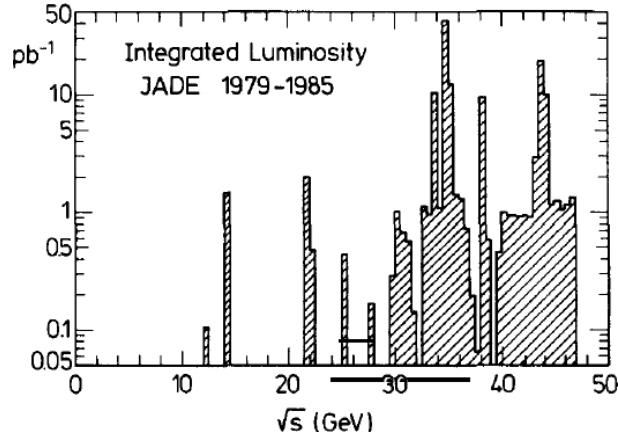


Figure 6.11: Integrated luminosity for the JADE experiment at PETRA

Reminder : e^+e^- kinematics One can write the differential cross section as,

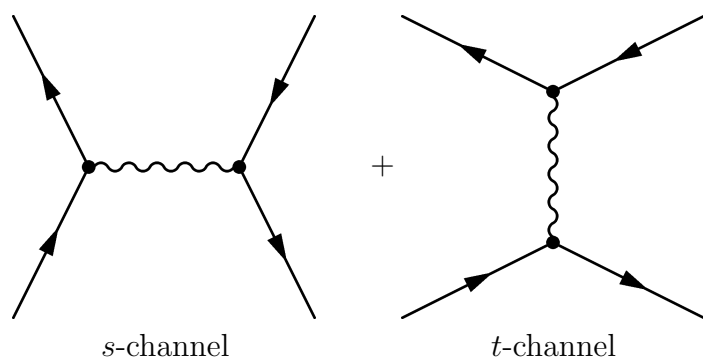
$$\frac{d\sigma_{\text{QED}}}{d\Omega} = \frac{d\sigma_0}{d\Omega}(1 + \delta_{\text{rad}}), \quad (6.9)$$

where δ_{rad} stands for the radiative corrections, i.e. terms coming from diagrams with more vertices (proportional to α in the case of QED). These include emission of further low energy exchange bosons and loop corrections.

6.2.4 Bhabha scattering

Leading order We first treat the leading order term, the one yielding $d\sigma_0/d\Omega$.

The following two diagrams contribute to the invariant amplitude :



Using Eq. (3.32) and the trace theorems of section 5.9, we get,

$$\begin{aligned} \frac{d\sigma_0}{d\Omega} &= \frac{\alpha^2}{4s} \left(\underbrace{\frac{t^2 + s^2}{u^2}}_{t\text{-channel}} + \underbrace{\frac{2t^2}{us}}_{\text{interference}} + \underbrace{\frac{t^2 + u^2}{s^2}}_{s\text{-channel}} \right) \\ &= \frac{\alpha^2}{4s} \left(\frac{3 + \cos^2 \vartheta}{1 - \cos \vartheta} \right)^2. \end{aligned} \quad (6.10)$$

Note that it is divergent for $\vartheta \rightarrow 0$. Fig. 6.12 shows the $\cos \vartheta$ -dependence of each component in Eq. (6.10). We remark that the differential cross section is dominated by the t -channel component at all angles, and that the s -channel is almost constant, when compared to the last. The interference term is always negative. It is small in magnitude for large scattering angles ($\vartheta \sim \pi \Leftrightarrow \cos \vartheta \sim -1$) and diverges in the case of forward scattering ($\vartheta = 0 \Leftrightarrow \cos \vartheta = 1$).

Fig. 6.13 shows the typical trace left in the electronic calorimeter by a scattered e^+e^- -pair. Fig. 6.14 shows $\sigma^{e^+e^- \rightarrow e^+e^-}$ measured as a function of $\cos \vartheta$ for different center of mass

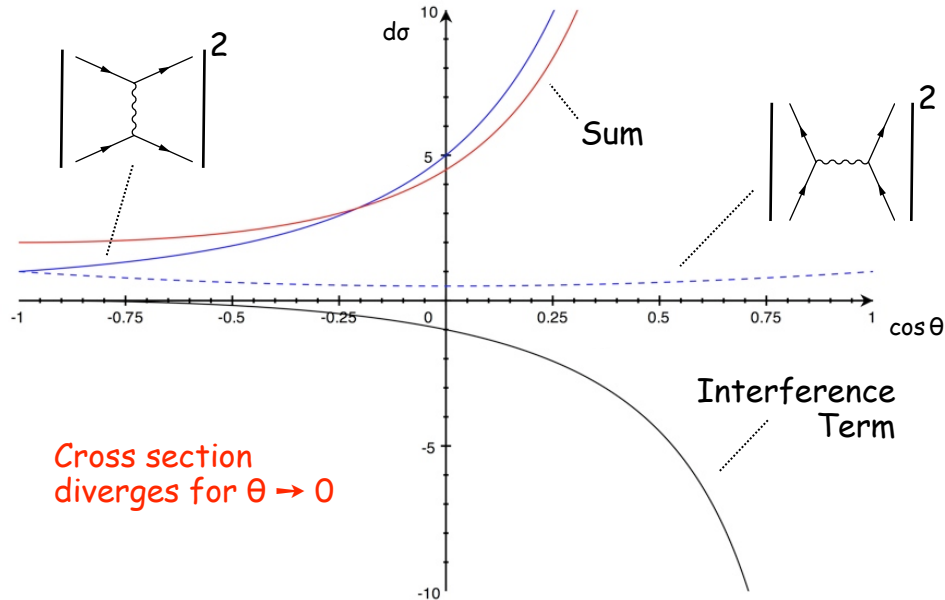


Figure 6.12: Relative magnitude of the different terms in $d\sigma_0/d\Omega$.

energies. It decreases following a $1/s$ -dependence.

Radiative corrections The diagrams contributing to the cross section and proportional to higher powers of α (or e) are shown in Table 6.2.

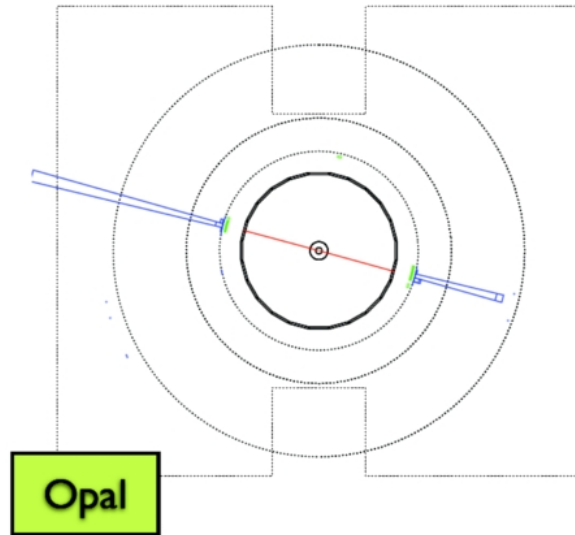


Figure 6.13: Typical event display of a Bhabha scattering event recorded by the Opal experiment. The length of the blue histogram corresponds to the amount of energy deposited in the electromagnetic calorimeter.

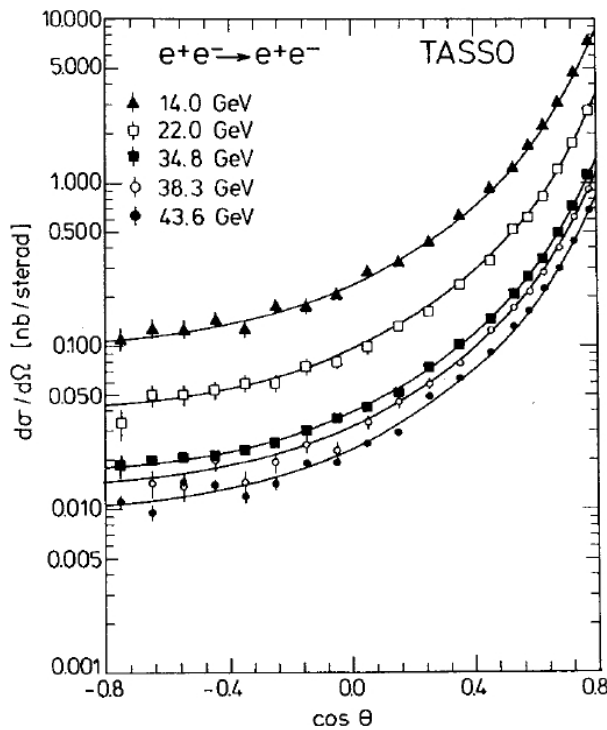


Figure 6.14: Energy and angle dependence of the cross section measured at TASSO and compared to leading order calculations.

$e^3 :$	
$e^4 :$	

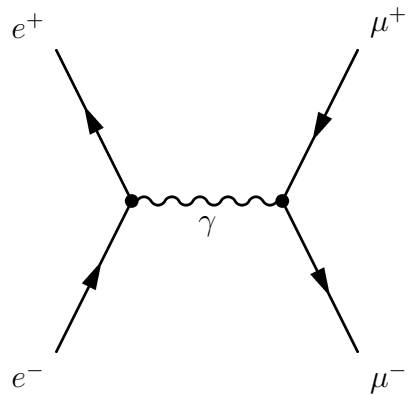
Table 6.2: Diagrams of radiative and loop corrections up to e^4

Because of momentum conservation, the diagrams of the e^3 -order imply that the electron-positron pair is no longer back-to-back after the collision. This effect is called **acollinearity**. The acollinearity angle is the angle $\xi = \pi - \phi$, where ϕ is the angle between the direction of the scattered electron and the scattered positron; for a back-to-back flight there is no acollinearity, thus $\xi = 0$. This angle has been measured at the JADE experiment and confirms higher order QED corrections in a very impressive way (see Fig. 6.15).

6.2.5 Lepton pair production

Muon pair production Looking at different final states gives also different results. We illustrate this by looking at the process $e^+e^- \rightarrow \mu^+\mu^-$. This is the simplest process of QED and is often used to normalize cross sections of other processes.

There is only one leading order Feynman diagram, namely,



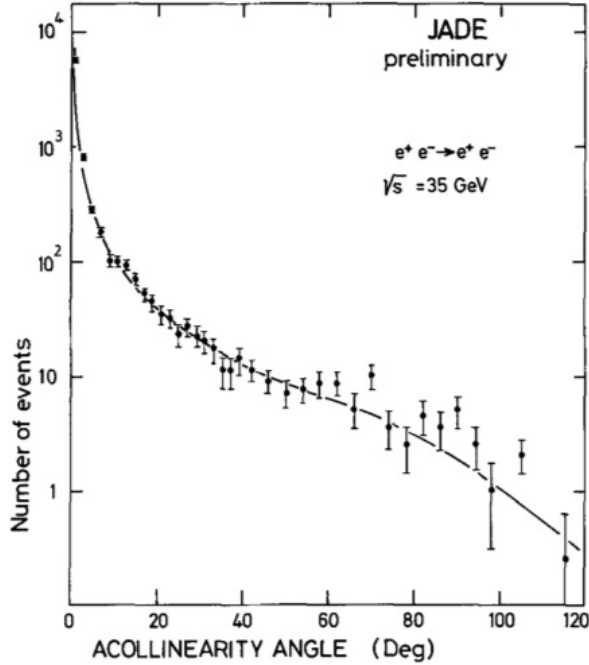


Figure 6.15: Comparison of measured acollinearity at JADE with the QED prediction.

and the leading order differential cross section is,

$$\frac{d\sigma_0}{d\Omega} = \frac{\alpha^2}{4s} \left(\frac{t^2 + u^2}{s^2} \right) = \frac{\alpha^2}{4s} (1 + \cos^2 \vartheta), \quad (6.11)$$

which is shown in Fig. 5.9.

Fig. 6.16 shows an event candidate: low energy deposits in the electromagnetic calorimeter and hits in the muon chambers.

Muon pair production : Z^0 exchange Since only s -channel contributes to the muon pair production, the diagram containing a Z^0 boson instead of a photon²,

²This contribution is also present in the case of Bhabha scattering, yet since the t -channel dominates over the s -channel, the effect is virtually invisible.

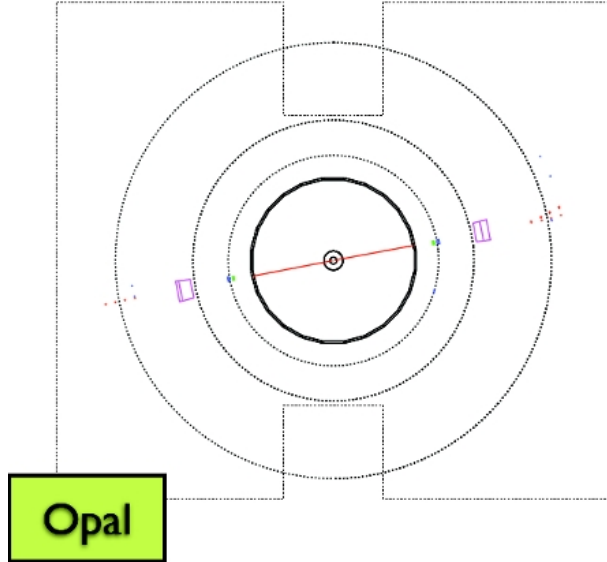
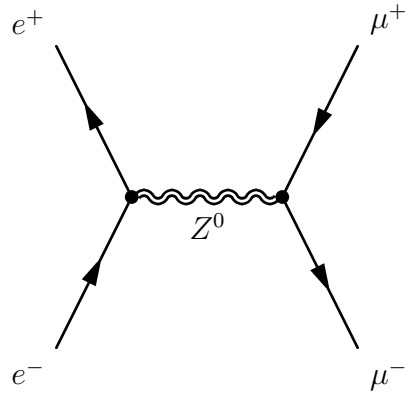


Figure 6.16: Typical event display of a muon pair production event recorded by the Opal experiment.



becomes comparable with the photon term (approx. 10%), even at leading order. This leads to a the modified cross section,

$$\frac{d\sigma_0^{\text{EW}}}{d\Omega} = \frac{\alpha^2}{4s} (1 + \cos^2 \vartheta + A \cos \vartheta). \quad (6.12)$$

This is illustrated in Fig. 6.17 comparing the QED and electroweak predictions to the data.

As an easy integration of Eq. (6.12) shows, the *total* cross section is not sensitive to the effects of electroweak interaction and we have a very good agreement with the QED value (Fig. 6.18).

For the \sqrt{s} -range measured at PETRA, electroweak corrections are small. In the case of LEP they are instead quite important, especially in the range around the Z^0 resonance,

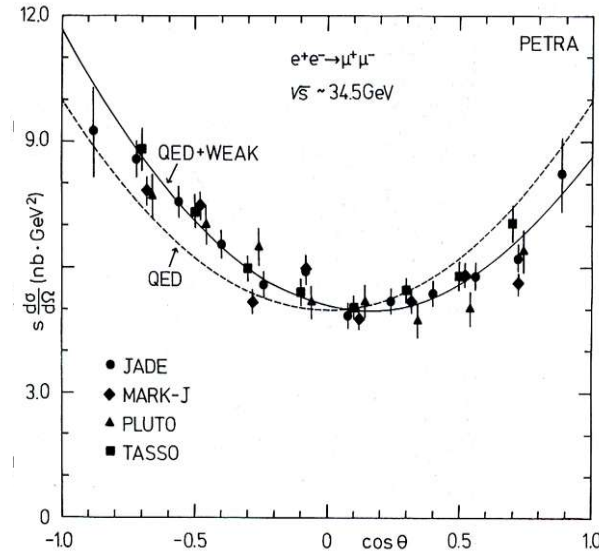


Figure 6.17: Comparison of $e^+e^- \rightarrow \mu^+\mu^-$ differential cross section measured at PETRA with the QED and electroweak predictions.

$\sqrt{s} \sim m_Z \approx 90$ [GeV].

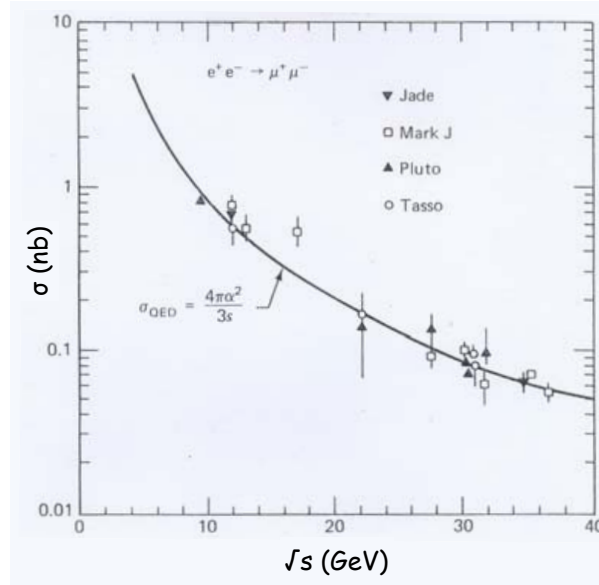
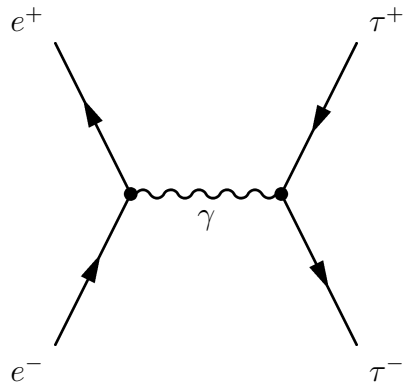


Figure 6.18: Comparison of measured total cross section at PETRA with the QED prediction.

Tau pair production At high enough energy ($\sqrt{s} \geq 2m_\tau \approx 3.6$ [GeV]) the production of $\tau^+\tau^-$ -pair – which is very similar to the case of muon pair production – is possible:



The final state of a tau pair production event observed in the detector can contain hadrons, since the lifetime of τ is very short ($\tau_\tau = 2.9 \cdot 10^{-13}$ [s]) and it is the only lepton with sufficiently high mass to produce $q\bar{q}$ -pairs.

Fig. 6.19 shows an event where one of the two tau survived long enough, e.g. because of a large energy and thus a longer lifetime $\gamma\tau_\tau$ in the laboratory frame, to hit the electromagnetic calorimeter, while the other one decayed in three pions which then left traces in the electromagnetic and hadronic calorimeters.

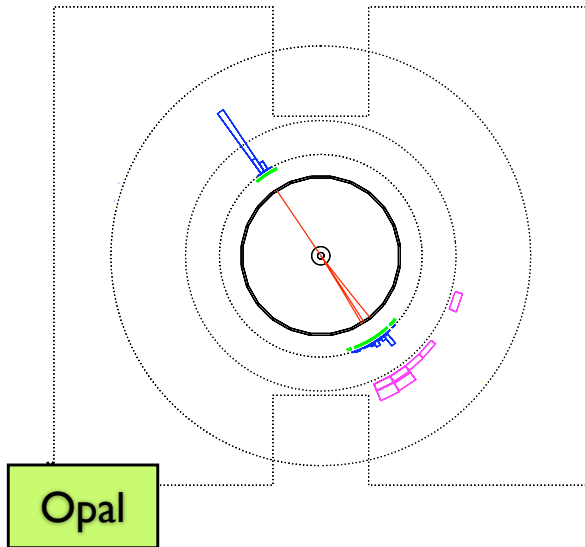


Figure 6.19: Typical event display of a tau pair production event recorded by the Opal experiment.

6.2.6 Hadronic processes

The production of quark-antiquark $q\bar{q}$ pair is another possible final state in e^+e^- annihilation.

When a bound $q\bar{q}$ state is produced, we speak of a **resonance** because the e^+e^- cross section looks like the amplification curve of a periodic system such as a pendulum or an RLC circuit near the resonant frequency. A famous resonance is the J/ψ resonance corresponding to a bound state of $c\bar{c}$.

Away from the resonances, there is in general no visible bound state, and the produced quarks hadronize in **jets** due to the confinement of the strong interaction : quarks cannot be seen as free particles.

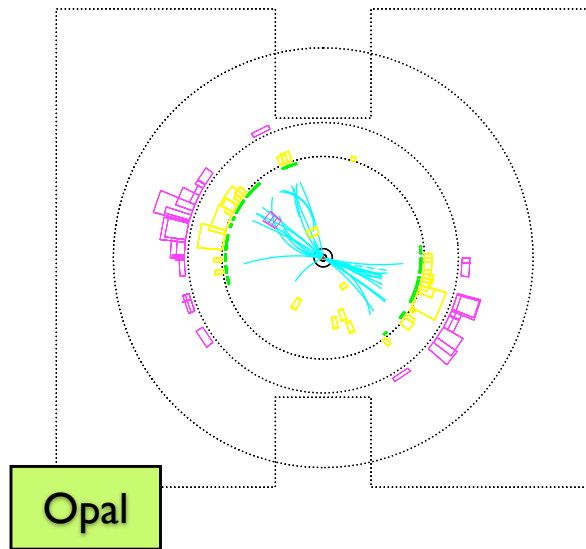
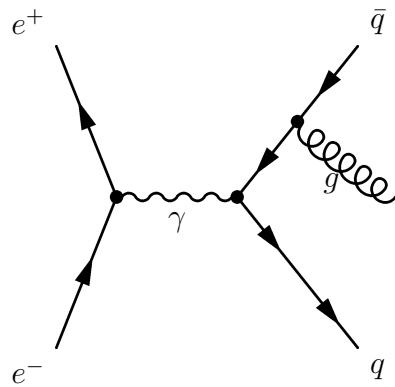


Figure 6.20: Typical display of jet production event recorded by the Opal experiment.

Due to the strength of strong interaction at low energy, the radiative effects (this time the radiated bosons are gluons),



take a much more dramatic form than in QED : Since gluons also have a color charge, they hadronize and for each emitted gluon one observes one more jet (Fig. 6.21).

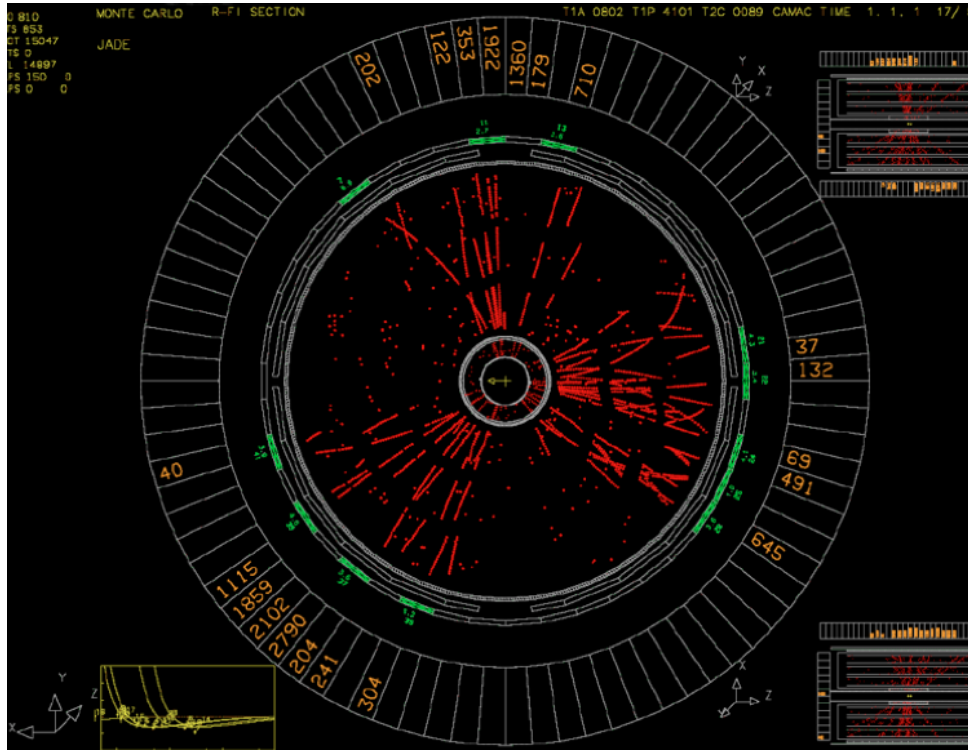


Figure 6.21: Typical event display of a 3-jets production.

6.2.7 Limits of QED

In this section, one addresses the question : what do we expect if QED is not the only theoretical model involved in the scattering processes discussed so far?

Suppose there is an energy scale Λ (equivalent to a length scale Λ^{-1}) at which QED does not describe the data anymore.

We would have changes of the various quantities, for instance, the potential, photon propagator and total cross section would be modified as follows :

$$\begin{aligned} \frac{1}{r} &\rightarrow \frac{1}{r} (1 - e^{-\Lambda r}) && \text{(potential)} \\ -\frac{1}{q^2} &\rightarrow -\frac{1}{q^2} \left(1 + \frac{q^2}{\Lambda^2}\right) && \text{(propagator)} \\ \sigma^{e^+e^- \rightarrow \mu^+\mu^-} &\rightarrow \frac{4\pi\alpha^2}{3s} \left(1 \pm \frac{s}{\Lambda^2 - s}\right)^2 && \text{(cross section).} \end{aligned}$$

The form of the potential is typical of a Yukawa coupling of a fermion with a massive spin 0 field. Since this particle is imagined as heavy – the energy available is smaller or similar to the production threshold Λ – we can treat this particle as spinless since spin effect are only significant in the relativistic case. This type of ansatz is thus standard in the sense that any new heavy particle that can be produced from an e^+e^- -annihilation will have the same effect on the potential, regardless of it being a scalar or a vector particle. The other quantities are then directly related to the change in the potential.

We have seen the electroweak effects to the QED cross section at the end of the previous subsection. This corresponds to $\Lambda \approx m_{Z^0}$ (Fig. 6.22).

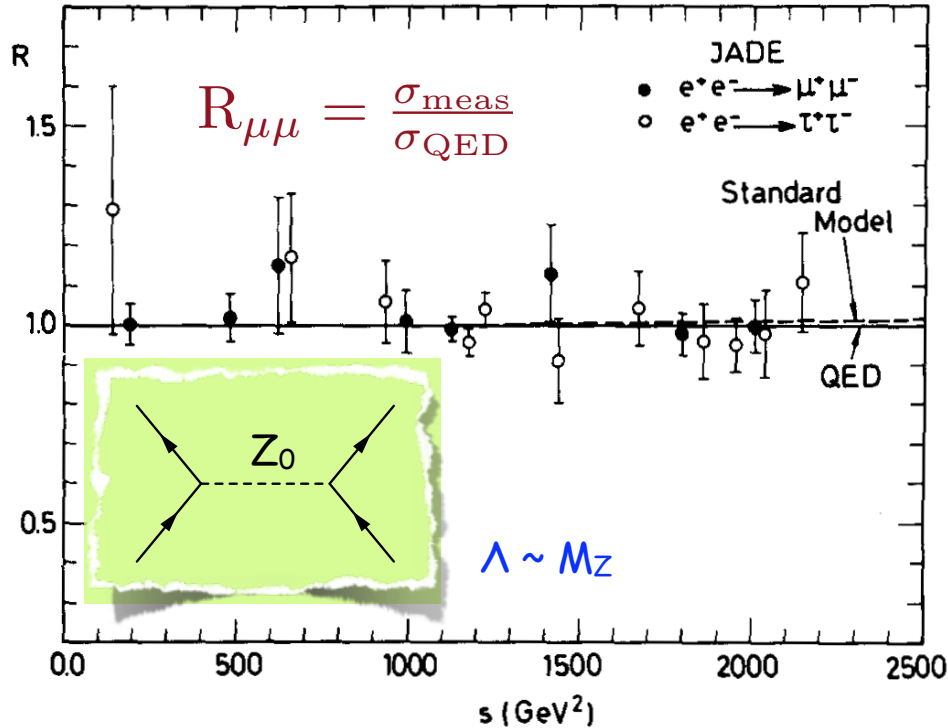


Figure 6.22: Comparison of measured total cross section at PETRA with the QED prediction for muon and tau pair production.

Fig. 6.23 shows the ratio,

$$R_{\mu\mu} = \frac{\sigma_{\text{meas}}^{e^+e^- \rightarrow \mu^+\mu^-}}{\sigma_{\text{QED}}^{e^+e^- \rightarrow \mu^+\mu^-}},$$

as measured at PETRA and TRISTAN. By comparing data and theory and varying Λ within the experimental error one can infer that – if any – new physics can only be brought in with a mass scale $\Lambda \geq 200$ [GeV].

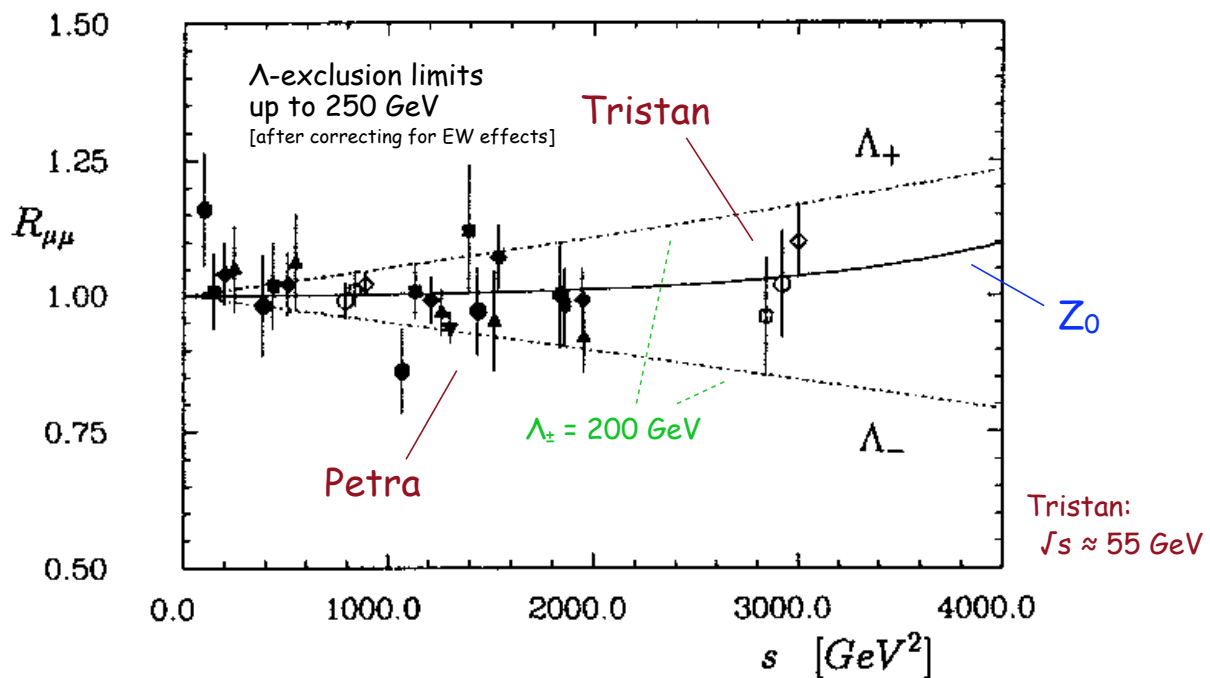


Figure 6.23: Comparison of measured total cross section at PETRA and TRISTAN with the QED prediction for muon pair production.